

Localized, Macromolecular Transport for Thin, Adherent, Single Cells Via an Automated, Single Cell Electroporation Biomanipulator

Kelly Sakaki, *Member, IEEE*, Hadi Esmaeilsabzali, Shabnam Massah, Gratien G. Prefontaine, Nikolai Dechev, *Member, IEEE*, Robert D. Burke, and Edward. J. Park*, *Member, IEEE*

Abstract—Single cell electroporation (SCE), via microcapillary, is an effective method for molecular, transmembrane transport used to gain insight on cell processes with minimal preparation. Although possessing great potential, SCE is difficult to execute and the technology spans broad fields within cell biology and engineering. The technical complexities, the focus and expertise demanded during manual operation, and the lack of an automated SCE platform limit the widespread use of this technique, thus the potential of SCE has not been realized. In this study, an automated biomanipulator for SCE is presented. Our system is capable of delivering molecules into the cytoplasm of extremely thin cellular features of adherent cells. The intent of the system is to abstract the technical challenges and exploit the accuracy and repeatability of automated instrumentation, leaving only the focus of the experimental design to the operator. Each sequence of SCE including cell and SCE site localization, tip-membrane contact detection, and SCE has been automated. Positions of low-contrast cells are localized and “SCE sites” for microcapillary tip placement are determined using machine vision. In addition, new milestones within automated cell manipulation have been achieved. The system described herein has the capability of automated SCE of “thin” cell features less than 10 μm in thickness. Finally, SCE events are anticipated using visual feedback, while monitoring fluorescing dye entering the cytoplasm of a cell. The execution is demonstrated by inserting a combination of a fluorescing dye and a reporter gene into NIH/3T3 fibroblast cells.

Index Terms—Electroporation, machine vision, microcapillary transfection, microelectrode, robot-assisted manipulation, single cell.

I. INTRODUCTION

TRANSPORTING proteins, DNA, and other metabolites across the cell membrane is a fundamental mechanism used to investigate human processes at the cellular level. However, the cell membrane forms an effective barrier to foreign molecules and alternative means are required to coerce entry [1]. One effective method of overcoming this barrier is single cell electroporation (SCE) via microcapillary, which can be applied to cells directly in culture or to tissue with minimal preparation. SCE, via microcapillary, is a highly localized, repeatable method for gene transfection and molecular uptake for both *in vitro* and *in vivo* single cell manipulation [2]–[6]. SCE induces reversible pores [7] in the membrane by channeling an electric field through a microcapillary [3], [8] and concentrating the electric field at the cell surface [see Fig. 1(a)]. Charged ions and molecules, contained within microliters of solution loaded in a microcapillary, are inserted through the pores via an iontophoretic flow and diffusion. Since the diameter of the tip is small, a high spatial selectivity of the cell and the location on the cell is achievable allowing the tip to be placed on extremely small cell features [4].

SCE is a versatile single cell manipulation method; however, the technical complexity limits its operation to highly trained operators. The complexities of single cell manipulation technologies in general, and the demand for more versatile instrumentation have coupled focused methods of molecular transport using robot-assisted technology. As a result, the capabilities of robot-assisted, single cell manipulation technologies, such as SCE and intracytoplasmic, and capillary pressure microinjection (CPM), have rapidly advanced over the last decade as single cell research evolves.

Robot-assisted manipulation of large, single cells and embryos in suspension (i.e., diameters on the order of 10^2 and $10^3 \mu\text{m}$'s) is frequently performed using intracytoplasmic injection techniques. This involves piercing through the cell membrane and using CPM to deliver molecules into the cytoplasm. Suspended cells can be immobilized with one microcapillary. Using visual servoing, a second microcapillary approaches and microinjects the cell in the same focal plane as the holding microcapillary [9]. Others have developed methods combining

Manuscript received March 12, 2013; revised May 23, 2013; accepted June 7, 2013. Date of publication June 12, 2013; date of current version October 16, 2013. This work was supported by the Natural Sciences and Engineering Research Council of Canada under Grant RGPIN/298219-2012 and Grant EQPEQ/406188-2011. The work of K. Sakaki was partly supported under the British Columbia Innovation Scholars Award. Asterisk indicates corresponding author.

K. Sakaki and H. Esmaeilsabzali are with the Faculty of Applied Sciences, Simon Fraser University, Surrey, BC V3T 0A3, Canada and also with the Faculty of Health Sciences, Simon Fraser University, Burnaby, V5A 1S6, Canada (e-mail: kelly.sakaki@sfu.ca; hesmaeil@sfu.ca).

S. Massah and G. G. Prefontaine are with the Faculty of Health Sciences, Simon Fraser University, Burnaby, BC V5A 1S6, Canada (e-mail: smassah@sfu.ca; ggpp1@sfu.ca).

N. Dechev is with the Department of Mechanical Engineering, University of Victoria, Victoria, BC V8W 3P6, Canada (e-mail: dechev@uvic.ca).

R. D. Burke is with the Department of Biochemistry and Microbiology, University of Victoria, Victoria, BC V8W 3P6, Canada (e-mail: rburke@uvic.ca).

*E. J. Park is with the School of Mechatronic Systems Engineering, Faculty of Applied Sciences, Simon Fraser University, Surrey, BC V3T 0A3, Canada, and also with the Faculty of Health Sciences, Simon Fraser University, Burnaby, V5A 1S6, Canada (e-mail: ed_park@sfu.ca).

Color versions of one or more of the figures in this paper are available online at <http://ieeexplore.ieee.org>.

Digital Object Identifier 10.1109/TBME.2013.2268387

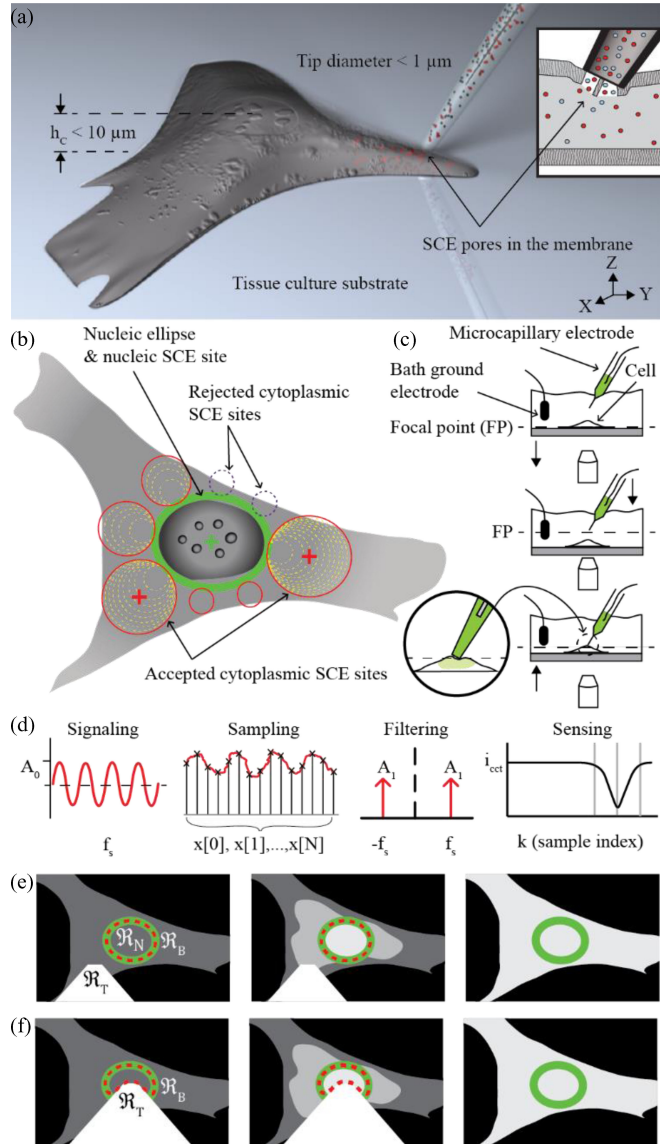


Fig. 1. Automated SCE. (a) Thin features on cells are targeted with microcapillary SCE to create (inset) reversible pores in the membrane used to insert molecules. (b) Nucleic and cytoplasmic SCE sites are localized on the cell using machine vision. (c) SCE site is positioned below the focal point and the tip is localized. The platform rises and brings the cell into contact with the tip. (d) Sinusoidal, sensing signal aids tip-membrane contact detection in the presence of a low SNR environment. Samples are input to the Discrete Fourier Transform. The signal is isolated on the frequency spectrum at f_s producing a measure of the current, i_{cc} , through the electrode to sense changes during tip-membrane contact. i_{cc} is relatively constant when the tip approaches the cell and abruptly decreases upon contact. This abrupt change is detected using statistical process control and tip motion is halted. Fluorescent molecules entering the cell via SCE are measured during (e) cytoplasmic and (f) nucleic SCE. A 1.5 times increase in fluorescent intensity in \mathfrak{R}_B (red boundary) signals an end to the SCE routine.

“sensing” capabilities, including machine vision and force data [8], [9]. Further, designs increased throughput by trapping embryos and suspended cells using suction ports [12] and grooves [10] fabricated directly into the substrate.

Manipulating single cells that have been trapped, or adhered to substrates typically require an out-of-plane [13] delivery method, and a framework of high precision instrumentation to

position a microcapillary on a cell with a cross-sectional height h_C as small as several micrometers. Conventional microscopy formats (e.g., upright and inverted microscopes) typically reduce the working environment to a 2-D image and impede the ability to visually detect tip-membrane contact. A CPM system attempted to overcome such challenges using machine vision to estimate the height of the microcapillary with respect to the position of adherent cells [14].

Alternatively, visual servoing methods can be substituted for, or combined with microcapillary-based, microelectrode measurements [3], [15]–[17], which sense the degree of “tip-membrane” contact as the tip indents the membrane. Decreasing the amplitude of a low-potential, sensing signal provides an indication of the seal created between the microcapillary tip and the cell membrane. However, in microcapillary-based methods, the resolution of the sensing signal used during the tip-membrane placement routine is hampered by a poor signal-to-noise ratio (SNR). This is common in electrode-based devices and was demonstrated in our previous work [18]. Large cells provide sufficient membrane deflection distance to achieve significant amplitude changes at a specified threshold beyond the SNR with classic filtering techniques. Therefore, a little chance of damage to the cell or the tip is likely. In contrast, thin cells 10 μm or less, are problematic where the distance from the tip to the membrane (i.e., tip-membrane) cannot be accurately resolved and the distance from the initial tip membrane contact to the substrate is small. Subsequently, the use of fixed-threshold contact methods [3], [15], [17] can impede operational throughput as a result of damaged tips, ruptured cell membranes, or false tip-membrane detections, especially where a low SNR is present.

Even after achieving significant advances in automated cell manipulation, the limitations with respect to the size of adherent cells has rarely been discussed. Microcapillary SCE can insert molecules into a cell without piercing the membrane and can be executed, while the microcapillary is in contact with the membrane surface [15], [17], [18] or positioned several micrometers away [8]. Where novel solutions have automated the full sequence or a partial sequence of the stages of SCE, greater efforts are required to localize and manipulate cells with thin cross sections and exploit one of the most significant advantages of microcapillary SCE.

Prior work has achieved significant milestones toward fully automated solutions. Rae and Levis [3] suggested a method of estimating the potential at the membrane during tip-membrane contact for SCE. In [15], a semiautomated solution for SCE was demonstrated by inserting fluorescing dye into aortic endothelial cells. Kallio *et al.*, provides an electrical model describing current flowing through the microcapillary and used microcapillary electrodes [16] to indicate contact in SH-SY5Y cells (mouse neural blastoma) using a CPM robot-assisted manipulator. He also describes conditions for detecting broken and clogged microcapillaries. Our laboratory provided an automated solution to localize and manipulate large, sea urchin eggs that were chemically adhered to a substrate [17] using SCE.

Although many technological milestones have been achieved in microcapillary-based SCE and similar technologies, further

advances are necessary where methods and designs in the literature fall short of, or have not been developed for an automated solution for the SCE of thin, adherent cells. The broad technical requirements and the fragile nature of cell structures limit the efficiency of manual-throughput and subsequently rates of processing are sufficiently slow [5], [6]. Furthermore, the full sequence of tasks have not been adequately achieved by automated efforts, thus the true potential of SCE has not been realized.

In this study, a novel system for fully automated SCE is described. Our system utilizes a machine vision algorithm, developed in our laboratory, to detect low-contrast, thin, adherent cells and SCE sites on cells for molecular delivery [19]. Applying SCE on the most suitable location of a cell is rarely discussed in experimental methods. Therefore, two sites were proposed and include the “nucleic SCE site” and the “cytoplasmic” SCE site [see Fig. 1(b)]. In addition, we demonstrate a more versatile and robust, tip-contact detection algorithm, based on statistical process control [18], for cells less than $10 \mu\text{m}$ in thickness. This achievement eliminates limitations imposed by thin, adherent cells and provides a transmembrane transport method for a much broader range of applications. Finally, an endpoint for SCE is estimated using visual feedback from fluorescing molecules that are inserted in and diffuse throughout the cytoplasm of a cell during SCE.

The operation of the system is demonstrated by inserting a fluorescent dye (Alexa Fluor Hydrazide 488) and a plasmid DNA with a reporter gene (pcDNA6-dsRed, 5.8 kbp) into NIH/3T3 fibroblasts. Two video demonstrations are provided as supplementary downloadable material and demonstrate the automation routine methodologies used in this study.

II. METHODOLOGY

A. Three Stages of Automated SCE

Automated SCE can be partitioned into three, sequential stages including, *Stage 1: cell localization and SCE site determination; Stage 2: tip-membrane contact detection, and Stage 3: SCE*, which is monitored using visual feedback.

Stage 1 (cell and SCE site localization): Cell and SCE site localizations were executed using a two-step algorithm [see Fig. 2]. First, the nucleus of a cell was localized and modeled as an ellipse, \mathcal{R}_N . The center of the ellipse determined the nucleic SCE site and the ellipse provided a bounded region \mathcal{R}_B , used to monitor visual feedback of the increase in fluorescent dye entering the cell during SCE. The localization of the cells and the corresponding SCE sites on the nucleus or cytoplasm was accomplished by first extracting the relatively high contrast features associated with the nuclei and surrounding rough endoplasmic reticula (RER) of cells in differential interference contrast (DIC) images. A sequence of an adaptive threshold and mathematical morphology operations coarsely located the nucleus of each cell. Next, each segmented nucleic region was estimated by an ellipse of similar geometrical and spatial properties. Fine localization of the nucleus was then realized using an iterative, *k*-means, clustering-based algorithm. Gradients associated with the nucleoli and other intranuclear organelles were

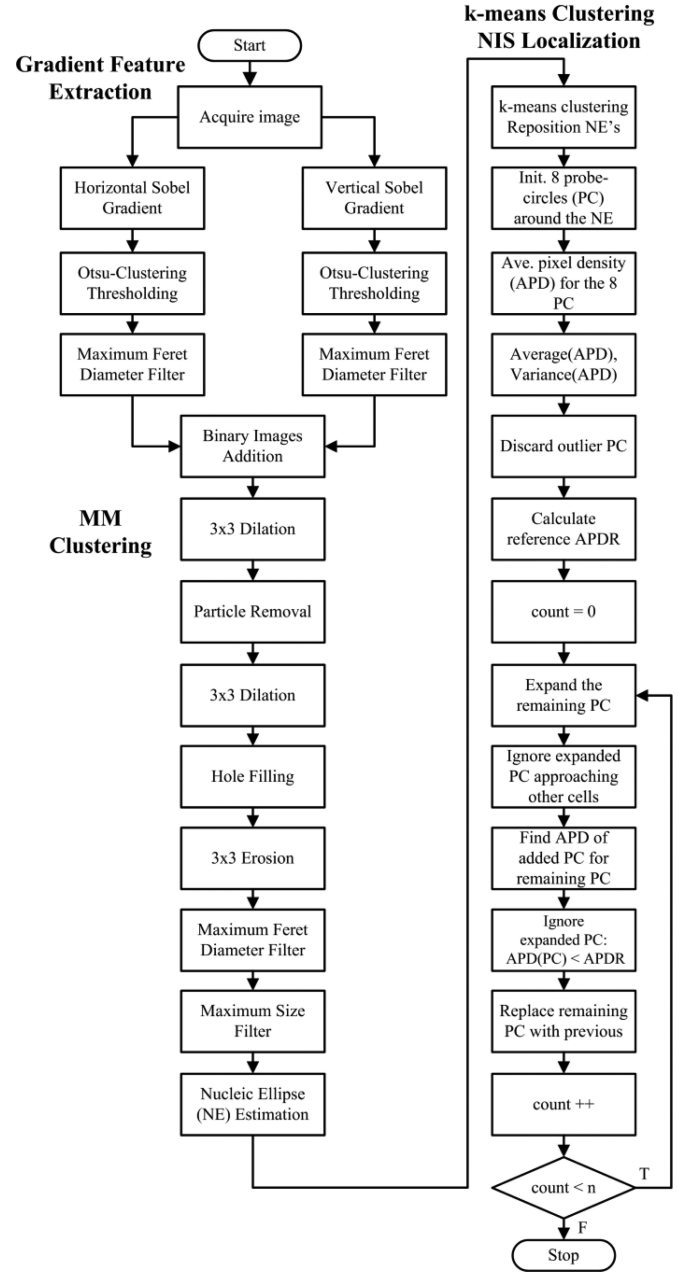


Fig. 2. Cell and SCE site localization. The gradient data associated with the nuclei and surrounding rough endoplasmic reticula in smoothed images is extracted and clustered to produce binary objects corresponding to each nucleus. Each binary object is then estimated with a nucleic ellipse (NE), and a *k*-means clustering algorithm iteratively repositions each NE until it encloses the nucleus. The final NE will be used to monitor the completion of SCE process, and its center may be selected as a nucleic SCE site. In the second stage, the Growing Circle Algorithm (GCA) uses a number of probe circles initiated around each NE to detect the cytoplasmic regions to the maximum extent possible. Upon completion of the GCA routine for each cell, the center of a probe circle that covers the thickest detected portion of the cytoplasm will be chosen as the cytoplasmic SCE site.

exploited in order to relocate the estimated nucleic ellipse in the image until \mathcal{R}_N enclosed the nucleus. Second, a modified region-growing algorithm called Growing Circles [19], used the results obtained during nucleic localization to localize the cell cytoplasm and determines a suitable SCE site over the cytoplasm

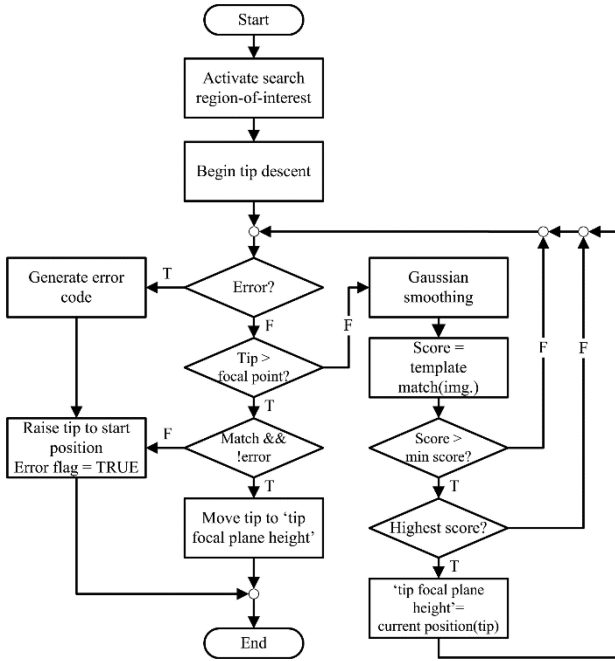


Fig. 3. Tip-template matching. Before the automation sequence begins, a microcapillary is attached to the platform for SCE. The tip is lowered to the focal plane and an image template is created and used for the duration of the automation. Prior to each tip-membrane approach, the tip is accurately located using template matching allowing placement of the tip on thin, cell features. The tip passes through the focal plane by several micrometers and template matching provides the highest correlation score obtained during the descent.

adjacent to the nucleus (i.e., cytoplasmic SCE site localization). Following localization of the cells and SCE sites, the cell is positioned 15 μm below the focal point [see Fig. 1(c)]. The tip descends to the focal point and was localized by using template-matching [see Fig. 3]. The SCE site on the localized cell is moved directly beneath the tip and ascends toward the tip at a constant velocity of 1 $\mu\text{m}/\text{s}$.

Stage 2 (tip-membrane approach sequence): Early detection of tip-membrane contact is a critical requirement for avoiding damage to thin cell structures and to the microcapillary, thus high resolution, tip-membrane placement is a requirement. Tip-membrane contact is achieved by detecting an abrupt decrease in measurements of the current i_{cct} through the microcapillary electrode. $S(t)$ is a low amplitude, sinusoidal “sensing signal” [see Fig. 1(d)], set at a fixed frequency, f_s . $S(t)$ is generated within a circuit that includes the microcapillary electrode, the cell bath solution, a cell bath electrode, and analog and digital circuitry used to measure and amplify the signal. Inherent noise, within electrode-based and electromechanical environments cause i_{cct} to fluctuate randomly about the mean of, i_{cct} , μ_0 , which is relatively constant during the tip-membrane approach.

Data are acquired in the basic form of discrete measurements

$$x_k = \theta_k + e_k \quad (1)$$

where x_k , is the k th measurement that includes θ_k the desired signal and e_k is the noise signal. These measurements are as-

sumed to be a sequence of n independent and random variables $(x_k)_{1 \leq k < n}$ with a mean value, μ_i .

In this study, x_k represents i_{cct} , the current measured through the electrode and μ_i is calculated using the cumulative moving average

$$\mu_i = \frac{1}{k+1} \sum_{k=1}^n x_{k+1} \quad (2)$$

and updated after each sample, k . At the start of the tip-membrane approach sequence, the standard deviation of i_{cct} measurements, σ , is acquired, while the tip is in motion and well before tip-membrane contact occurs (i.e., while i_{cct} is relatively constant).

The standard deviation provides a measure of the SNR,

$$\text{SNR} = \frac{\mu_1 - \mu_0}{\sigma} \quad (3)$$

and defines the signal level required to discern a change beyond the noise about the mean, μ_0 . In this study, μ_0 is calculated as the average of the cumulative sum using (2). The residual (i.e., the difference between the measured data and the average), $x_k - \mu_i$, is normalized with σ ,

$$y_k = \frac{x_k - \mu_i}{\sigma} \quad (4)$$

then y_k is input to the double-sided, cumulative sum [20] or “cusum”—a statistical process control algorithm. The cusum defines two recursive statistics, C_k^+ and C_k^- as follows:

$$C_k^+ = \max [0, C_{k-1}^+ + y_k - \lambda] \quad (5)$$

$$C_k^- = \max [0, C_{k-1}^- - y_k - \lambda] \quad (6)$$

where λ is the slack variable. The value of C_k^+ or C_k^- increases when $y_k > \lambda$ or $-y_k > \lambda$, respectively. If an abrupt change in one direction occurs, an alarm d is signaled when either C_k^+ or C_k^- exceeds the threshold ν ,

$$d = \begin{cases} 0 & \text{if } C_k^+ < \nu \cap C_k^- < \nu \\ 1 & \text{if } C_k^+ \geq \nu \cup C_k^- \geq \nu. \end{cases} \quad (7)$$

A sharp decrease in i_{cct} is observed when tip-membrane contact occurs causing C_k^- to exceed ν signaling a tip-membrane contact condition. Should C_k^+ exceed ν , an alarm is activated indicating a faulty electrode or broken tip. The values of λ and ν are set relative to σ and are discussed in Section II-B. Greater detail on the tip-membrane approach sequence can be found in [18]. A full statistical analysis on the cusum and the parameters are discussed in [20]–[23].

Stage 3 (SCE): Following tip-membrane contact detection, a low duty-cycle, square wave pulse initiating SCE is activated. Fluorescent molecules enter the pores induced by SCE at lower potentials than for larger molecules (e.g., plasmid DNA) and serve as a mechanism to correlate the transmembrane transport of molecules. SCE event detection is monitored by analyzing changes in the relative fluorescent intensity within a bounded region \mathfrak{R}_B in the cell using machine vision [see Fig. 4].

The averaged fluorescent intensity I_k within \mathfrak{R}_B is acquired and compared to the background or initial average fluorescent

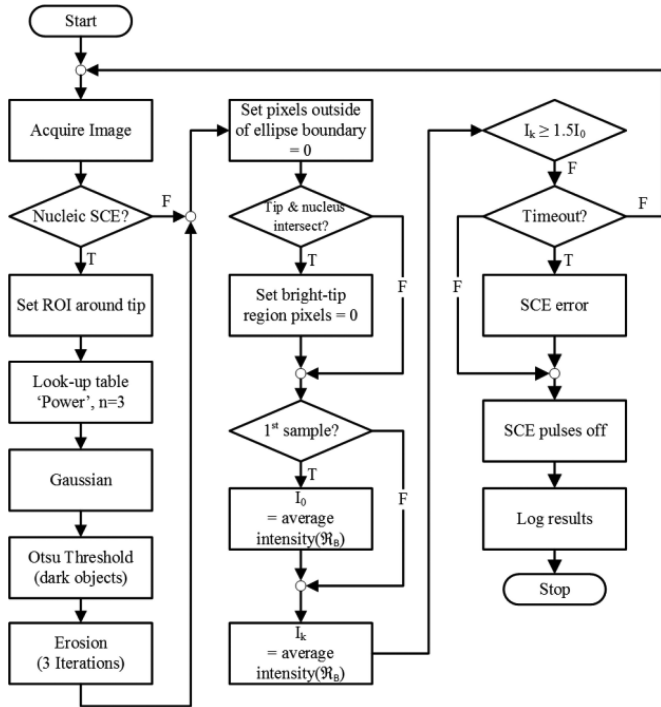


Fig. 4. SCE detection using visual feedback. Nucleic and cytoplasmic SCE are observed, while measuring increases in fluorescent intensity inside the cell during SCE pulses. If nucleic SCE is being performed, the image is applied to a power, lookup table to increase the pixel intensity of the fluorescent tip. This result provides a well-defined area where pixels are saturated due to the fluorescing tip. The tip region, \mathfrak{R}_T , can then be removed from the nucleic ellipse, \mathfrak{R}_N , using Otsu clustering where overlap of \mathfrak{R}_T and \mathfrak{R}_N occurs during nucleic SCE. In both cytoplasmic and nucleic SCE, measurements of the average fluorescent intensity, I_k , in \mathfrak{R}_B can then be acquired and compared to the initial fluorescent intensity I_0 , measured at the beginning of the routine.

intensity I_0 measured prior to SCE. In addition, a SCE endpoint threshold set to $1.5I_0$ was used in this study. When I_k exceeds this threshold, a signal is issued indicating that SCE is complete. Relative fluorescence intensity measurements occur concurrently as SCE pulses are applied. Analyzing the increasing pixel average I_k during electroporative pulses within \mathfrak{R}_B provides an indicator that SCE is occurring.

The nucleic and cytoplasmic SCE routines execute similarly with the exception of nucleic SCE, where the brightly fluorescing tip is excluded from fluorescence measurements. \mathfrak{R}_B is represented by one of two bounded regions depending on the type of SCE site selected and are defined for cytoplasmic SCE sites [see Fig. 1(e)] by

$$\mathfrak{R}_B = \mathfrak{R}_N \quad (8)$$

where \mathfrak{R}_N is the localized nucleus, and for nucleic SCE sites [see Fig. 1(f)] by

$$\mathfrak{R}_B = \mathfrak{R}_N \wedge \overline{\mathfrak{R}_T} \quad (9)$$

where \mathfrak{R}_T is the bounded region of the fluorescent tip. A rectangular, region of interest surrounding the location of the tip and the entire nucleic ellipse is applied to an exponential lookup table to increase the regions of high fluorescent intensity. The

resulting output was input to an Otsu threshold routine (i.e., clustering) to remove \mathfrak{R}_T from \mathfrak{R}_N and was followed by an erosion operation. This effectively reduces dispersion effects of the gradient between \mathfrak{R}_T and \mathfrak{R}_N effectively leaving the remainder of \mathfrak{R}_N for analysis.

B. Tip-Membrane Approach and Cusum Initialization

Prior to routine operation, a system calibration routine was performed to estimate suitable values for the threshold ν and the slack variable λ . Adjustments to λ and ν affect the indentation depth of the tip and the cusum algorithm's sensitivity to noise. In general, decreasing λ reduces the indentation depth (i.e., number of samples) before tip-membrane contact detection, but increases the possibility of generating a false tip-membrane contact alarm. Increasing ν gradually increases the indentation depth before detecting tip-membrane contact. The value of σ is estimated at the beginning of each tip-membrane approach sequence.

Six calibration test-runs were performed. Each test-run consisted of executing the tip-membrane contact detection routine to collect i_{cct} data on sample cells with the exception that the tip indentation continued until tip-breakage occurred. Three test runs were executed with the center of the nucleic ellipse as the target and three test runs were performed with the cytoplasmic SCE site used as the target. Sequential i_{cct} data were collected during the approach sequence, during tip-membrane contact (i.e., abrupt decrease in i_{cct}), and during the tip-substrate contact (i.e., abrupt increase in i_{cct}). SCE was purposely omitted throughout these runs.

Following the calibration test runs, offline simulations were performed on the i_{cct} datasets. Each i_{cct} dataset was input to the cusum routine and an iterative routine, described in [18], which stepped through each pair of ν , and λ to evaluate where the cusum would signal an alarm condition. The parameter pairs of λ and ν varied over a wide range to determine suitable pairs for operational use. In this study, the range of values for λ and ν was $[-0.1, 30]$

After each pair was tested by the iterative routine, a contour plot (i.e., performance surface) was generated using the indentation distances over the $\lambda-\nu$ parameter space. Lower indentation values were generated directly after tip-membrane contact first occurred (i.e., transition from the constant i_{cct} to the abrupt decrease of i_{cct}) and before the tip contacted the substrate (i.e., before the abrupt increase in i_{cct}). Pairs that caused a false tip-membrane contact detection, pairs that failed to detect contact before the tip contacted the substrate, or pairs that did not detect contact at all were assigned a high indentation value to indicate unsuitable parameters. In this study, a value of $20 \mu\text{m}$ was assigned to these pairs, which is greater than twice the average height of the cells measured [18]. The three runs of each group were averaged producing two contour plots—one for the nucleic runs and the other for the cytoplasmic runs shown in Fig. 5(a) and (b), respectively. In this study, parameters for operational use were selected such that the indentation was approximately $1.5 \mu\text{m}$ in depth ($\lambda = 20$, $\nu = 4$).

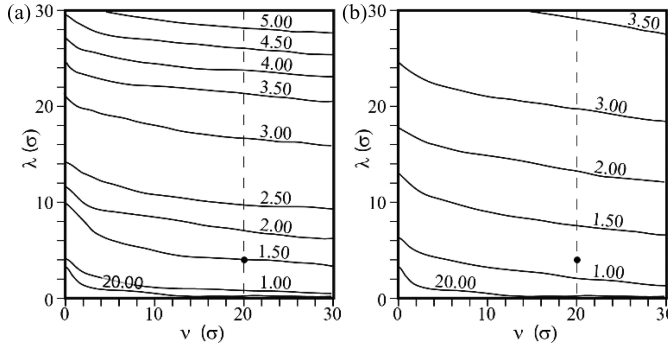


Fig. 5. Performance surface plots generated for the tip-membrane calibration runs. (a) Surface generated for nucleic and (b) cytoplasmic SCE sites. Each plot was generated using the i_{cct} data during three tip-membrane approach sequences. Each set of i_{cct} data is tested once for each pair of parameters (ν, λ) during an offline analysis producing an estimated indentation depth. Plotting the indentation depths over the range of parameters produced a performance surface allowing the selection of suitable system parameters for use. In this study, parameters were chosen such that the tip indentation was approximately $1.5 \mu\text{m}$ ($\nu = 20, \lambda = 4$). Contour units are in μm .

C. Experimental SCE Parameters

The automated routine was validated using two sets of parameters for nucleic and cytoplasmic SCE. A pulse width of 1 ms was used in all sets. Two pulse frequencies, 10 and 40 Hz were used in combination with an SCE pulse potential, V_{SCE} , of -6 and -10 V for nucleic SCE. These parameters have been demonstrated using manual methods of SCE [3]; however, the SCE site in [3] was not specified. For cytoplasmic SCE, only a V_{SCE} of -6 V was used as high potentials and high frequencies adversely affected the NIH/3T3 cells (e.g., -10 V and 40 Hz). A complete analysis relating the efficiency of the SCE parameters, SCE site location, and uptake of electroporated molecules were not the focus of this study.

D. SCE Biomanipulator Platform

The custom platform [see Fig. 6(a)] consisted of an X , Y , and Z linear, direct-drive platform (ALS 1000, Aerotech, Inc.). Each stage was powered by an Aerotech BA-10 amplifier and submicrometer precision was obtained using MXH-500 high-resolution, encoder signal multipliers. Aerotech drivers were interfaced to a National Instruments (NI) NI-7358 and two NI UMI-7774 interfaces. Software control of the motors was performed using the LabVIEW Motion API.

A custom optical train integrating Nikon CFI-60 and DIC elements consisted of a 40X, extra-long working distance objective. Fluorescence observation was performed using epifluorescence illumination with a red filter (Chroma Technology Corp. 49008/ET-Texas Red) for the dsRed and green filter (Chroma Technology Corp. 49002/ET-GFP) for the Alexa Fluor 488, respectively. All images were captured using a 12-bit CCD camera (Retiga, QImaging) at a maximum rate of 10 frames/s using two-times binning.

E. System Control Architecture

The system control software was structured using supervisory control with the automation core designed as a queued state-machine [see Fig. 6(b)] using LabVIEW 2011. Submodules were used to collect data from independent peripherals and execute low-level processing. Information compiled by the submodules was returned to and was collectively processed by the supervisory module. Data transfer latency between the submodules and the supervisory module and the time of the data spent in the queue was negligible.

F. SCE Module

The SCE module is an embedded system designed to generate signals, acquire i_{cct} measurements indicating tip-membrane proximity, and deliver electroporative pulses to induce SCE. The SCE module is comprised of three submodules including the signal generator, the data acquisition module (DAQ), and the data processing module which is integrated into the supervisory module. Signal acquisition and signal generation occurred near the microcapillary. The block diagram is shown integrated into the system control architecture in Fig. 6(b).

A digital signal processor (DSP, Microchip dsPIC 30f3013, Microchip Technology) and LabVIEW coordinated using serial, asynchronous communications at 19.2 kb/s. Signal generation was completed by the DSP, which sent 16-bit words, representing the voltage, to a 16-bit digital-to-analog converter (DAC, Analog Devices AD660) over an 8-bit bus. The DAC output a signal of up to ± 10 V and was amplified by 1.8 times providing a maximum amplitude pulse of ± 17.3 V to the electrode. Hardware filters were avoided to maintain a wide bandwidth reducing pulse signal distortion.

Two signals were generated during the automated sequence. During the tip-membrane approach sequence, $S(t)$ was generated with a peak amplitude, A_0 , of $0.3 V_p$ and at a frequency f_s of 186 Hz. Following tip-membrane contact detection, a unipolar, rectangular wave pulse at a potential of V_{SCE} was activated in order to induce SCE. The low potential sensing signal was applied intermittently between pulses to acquire measurements of i_{cct} during SCE by combining the two signals at the output.

The sensing signal and the pulses for inducing electroporation were output from the DAC to a discrete network of amplifiers in a current-to-voltage (C2V) configuration, and provided a measure of i_{cct} through the electrode. The output of the instrumentation amplifier was reduced to a maximum ± 10 V and was sampled by a NI USB-6009 DAQ at 44 kHz.

Raw data samples of the sinusoidal signal were transferred to LabVIEW in 712 sample windows and were analyzed using the discrete Fourier transform (DFT). The resulting i_{cct} amplitude of the sinusoidal signal, representing x_k in (1), was conveniently isolated on the frequency spectrum at f_s using the DFT. The value of u_0 was updated in (2). x_k was normalized with σ in (4) and output at a rate of 25 Hz to the cusum in (5) and (6), while checking for alarm conditions in (7).

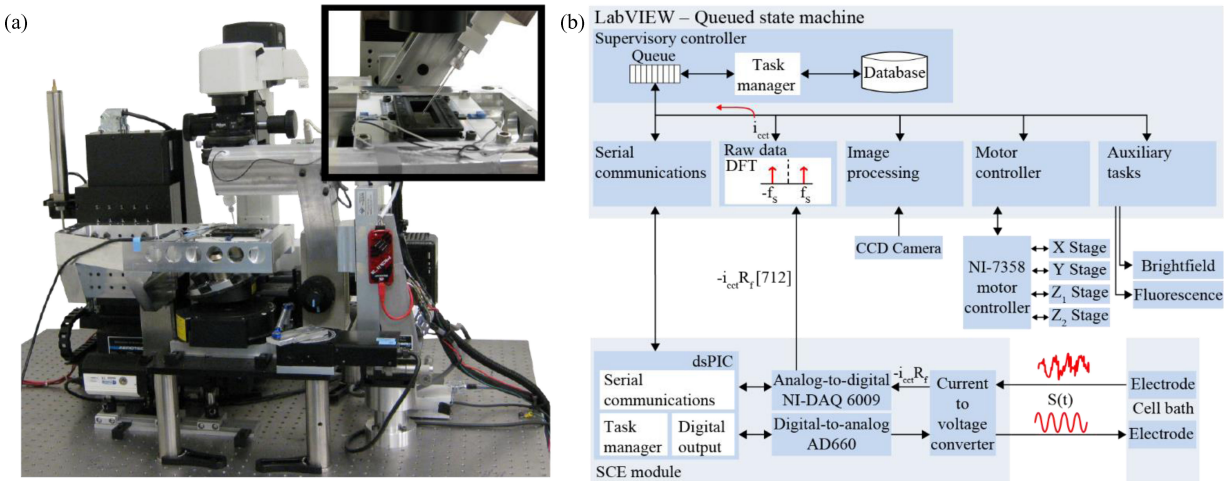


Fig. 6. SCE biomanipulator. (a) Biomanipulator used during experimentation to conduct automated SCE. (inset) A view of the cell chamber and the microcapillary used for SCE during the automated routine. (b) Hardware and software system block diagram.

G. Microcapillaries and Microelectrodes for SCE

Microcapillaries were fabricated on a Flaming/Brown P-97, using fire polished microcapillaries (Sutter BF150-110-10) and the “bee-stinger” protocol [24]. Microcapillaries were backfilled with a 4 μL solution containing 63 ng/ μL dsRed plasmid [25], 150 mM KCl, and 3.8 mM Alexa Fluor 488.

The electrode was fashioned by immersing 0.25-mm diameter silver wire (64-1319, Harvard Apparatus) in bleach for 30 min until an even coating of silver-chloride coated the bare wire. This wire was cleaned with 70% EtOH, washed with distilled water, and allowed to dry. The microcapillary was inserted in an electrode holder (1-HL-U, Molecular Devices) and the tip of the wire was immersed beyond 2 mm of solution from the end of the microcapillary. The electrode assembly was then inserted on the SCE module. After experimentation, the electrode wires were sufficiently rinsed with 70% EtOH followed by distilled water and allowed to dry.

H. Cell and Reagent Preparation

NIH/3T3 cells (ATCC #CRL-1658) were cultured in alpha Modified Eagle Medium (α -MEM, Invitrogen, 32571-028) supplemented with 10% fetal bovine serum (FBS, Invitrogen, 16000-036) and 1% Penicillin–Streptomycin (Invitrogen, 15140-122).

For the purpose of experiments and to achieve high-resolution imaging, the cells were prepared and cultured in a coverslip bottom, cell chamber [Quorum Technologies, Chamilde, WL-2460-1, Fig. 6(a, inset)]. The complete cell chamber assembly, including a No. 1.5, 24 \times 60 mm coverslip (VWR, CA48383-252-1), were autoclaved prior to use. Cells were cultured in 100 mm Petri dishes for 72 h. At 90% confluence, the cells were rinsed with phosphate buffered saline (PBS) and treated with 0.4 mL of 0.25% Trypsin-EDTA for 1 min in 37 °C. After detachment, the cells were diluted by culture media to 8 mL. The concentration of the diluted cell solution was further reduced by addition of the culture media in a 1:10 volumetric ratio. The final cell solution was added to the cell chambers and incubated for

24 h prior to experimentation. Following the incubation period, the cells were rinsed three times with PBS followed by adding fresh media (Invitrogen, 41061-029—no phenol red). The cells were placed back in the incubator for 3 h prior to experimentation. Following the incubation period, a cell chamber was placed on a custom cell heater on the robotic platform. A dual temperature controller (Warner Instruments, TC-344B) was connected to the cell heater maintaining the temperature at 37 °C. Cells remained viable for durations greater than 30 min; however, were kept outside the incubator for no longer than 20 min at a time. 10–15 cells were processed during each round of experimentation and were incubated for 24 h prior to inspection.

III. RESULTS

The automated SCE sequence was completed for 200 nucleic SCE and 100 cytoplasmic SCE runs. Examples of data acquired during automation of each type of sequence are shown in Fig. 7. A video demonstration is also provided and shows several cells and SCE sites being localized and then processed using the automated routine (Video 1—supplementary information).

In Fig. 7(a), a localized cell selected for nucleic SCE during *Stage 1*, is shown in *Image i*. The initial localized nucleus ellipse is shown as a green outline around the nucleus. During the tip-membrane approach sequence [see Fig. 7(a)] of *Stage 2*, i_{cct} measurements were constant until the tip-membrane contact was detected (*Image ii*) after approximately 1.3 μm of indentation. An abrupt increase in C_k^- can be seen in Fig. 7(b) as i_{cct} samples decreased in value during contact. At that moment, epifluorescent illumination was activated (see *Image iii*) and the bright fluorescing tip region \mathfrak{R}_T was removed from \mathfrak{R}_N allowing increases in fluorescing intensity to be monitored in \mathfrak{R}_B during SCE. During the SCE pulses in *Stage 3*, relative measurements of the fluorescent intensity within the nucleus increased linearly [see Fig. 7(c)] to the threshold, $1.5I_0$ ending SCE pulses. The change in fluorescent intensity can be observed in coarse pixel plots before SCE pulses begin (see *Image iv*) and directly before SCE pulses end (see *Image v*). The minimum intensity in the 8-bit images is 0 (dark blue) and the maximum pixel intensity

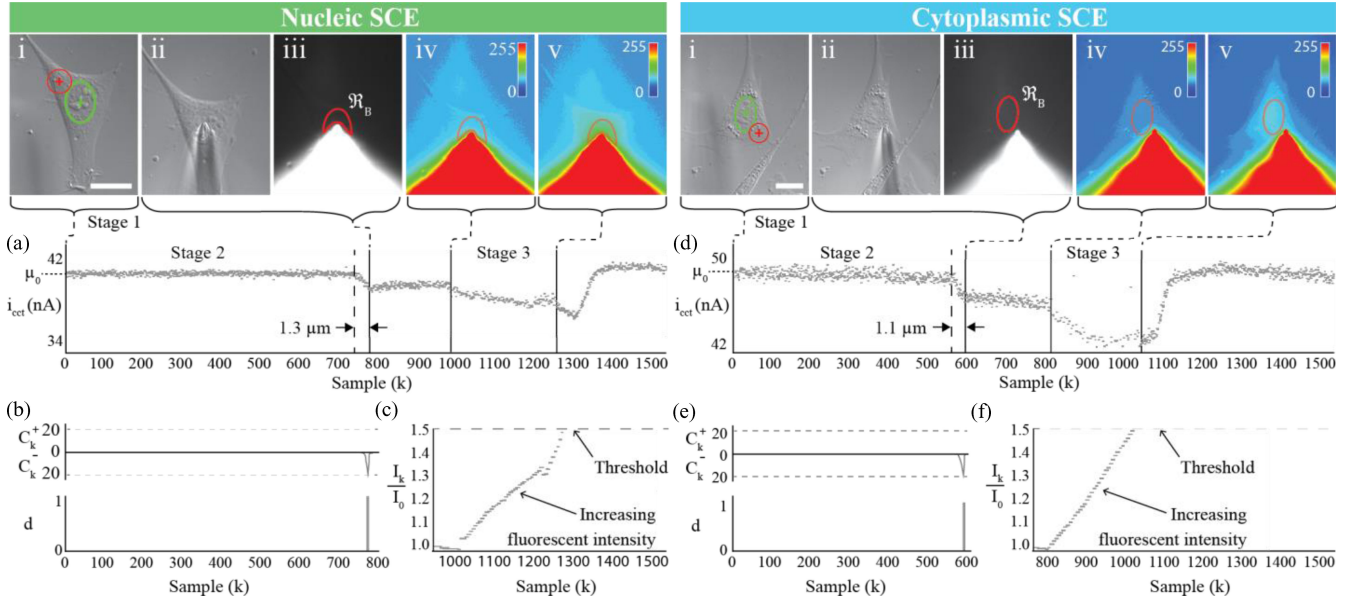


Fig. 7. Examples of the automation SCE sequence. During *Stage 1* nucleic and cytoplasmic SCE sites are localized in *Image i*. (a) i_{cc} samples are shown during the tip-membrane approach sequence (*Stage 2*). (b) During tip-membrane contact, shown in *Image ii*, i_{cc} samples, in (a), decreased from the average current, μ_0 and the negative cusum exceeded the threshold signaling an alarm, d , after an estimated indentation of $1.3 \mu\text{m}$. Epifluorescent illumination was activated in *Image iii* and the average fluorescent intensity in \mathfrak{R}_B was measured during SCE pulses. (c) During SCE pulses, relative fluorescence measurements, I_k / I_0 , increased in a linear fashion until the fluorescence intensity reached $1.5 I_0$. Coarse pixel intensity plots are shown in *Image iv*, before pulses began, and in *Image v*, immediately before pulses ended. Similar results are seen for cytoplasmic SCE in (d–f).

TABLE I
TIP-MEMBRANE CONTACT AND FLUORESCENT DYE DETECTION
SUCCESS RATIOS

SCE Site	Tip-membrane contact		Fluorescent dye detection	
	N	Tip-membrane contact success %	N	Fluorescent dye detection success %
Nuc	200	98.5	197	96.5
Cyto	100	99.0	99	86.9

is 255 (red). Following SCE, in *Stage 3*, the tip is raised and i_{cc} returns to the level at the onset of *Stage 2*. Similar data from a sequence for cytoplasmic SCE are shown in Fig. 7(d–f). In Video 2 (supplementary information), the SCE sequences are shown for the nucleic and cytoplasmic SCE datasets from Fig. 7.

In all cells localized for both nucleic and cytoplasmic SCE, tip-membrane contact detection was successful without tip-breakage and 98.8% successful in tip-membrane placement ($N = 300$)—failed runs occurred due to pierced cells and pierced cells exhibited dye immediately prior to SCE pulses (see Table I). The processing time for each run was an average of 81 s per cell. During the tip-membrane placement routine, the average σ measured was 0.44 nA ($SD = 0.38$ nA, $N = 300$) and the average i_{cc} measured at the beginning of the run was 39.9 nA ($SD = 10.6$ nA, $N = 300$). A total of 24 microcapillaries were used and fabricated using identical “pulling” parameters [24].

When the microcapillary was placed over the nucleus, a success rate of 96.5% electroporation of the dye was achieved ($N = 200$) and was 19.0% successful at transfection and expression of plasmid DNA for all cells. However, when regions lateral to the nucleus are targeted (i.e., cytoplasmic sites), a success rate of 86.9% electroporation of the dye is achieved and no successful

TABLE II
DsRed TRANSFECTATION RATIO 24 h AFTER SCE

Set	SCE Site	N	Pulse freq. (Hz)	V _{SCE} (V)	t _{SCE} (s)	t _{SCE SD} (s)	dsRed %
1	Nuc	50	10	-6	11.1	9.0	10.0
2	Nuc	50	40	-6	4.6	4.8	44.0
3	Nuc	50	10	-10	5.3	3.0	2.0
4	Nuc	50	40	-10	2.1	6.1	20.0
5	Cyto	50	10	-6	14.1	9.2	0.0
6	Cyto	50	40	-6	11.6	8.8	0.0

transfection of plasmid DNA ($N = 100$). The average elapsed time during SCE pulses measured for I_k to reach $1.5 I_0$ and the success ratio of detecting dsRed in cells following 24 h after SCE is t_{SCE} and summarized in Table II for each parameter set.

A followup study was performed in the absence of viability data validating cytoplasmic SCE due to the lack of dsRed expression in all cells. Cytoplasmic SCE site sequences were repeated for 20 trials. Following cytoplasmic SCE, cells were monitored over a 24-h period and image data were acquired in 6 h intervals to ensure the viability and the continuity of the location of the cells [see Fig. 8]. Continuity of the cells’ location was observed by monitoring bright field images [see Fig. 8(a–e)] and fluorescent microscopy images of the fluorescent dye over a 24-h duration [see Fig. 8(f–i)]. Following the 24-h period, the media was replaced with media containing calcein-AM red. After incubating the cells in calcein-AM for 1 h in 37°C , the media was replaced with media without calcein-AM. The cells were then inspected using epifluorescent microscopy and cells fluorescing under a red filter indicated cell viability [see Fig. 8(j)]. For all cells, the average viability was 60% ($N = 20$)

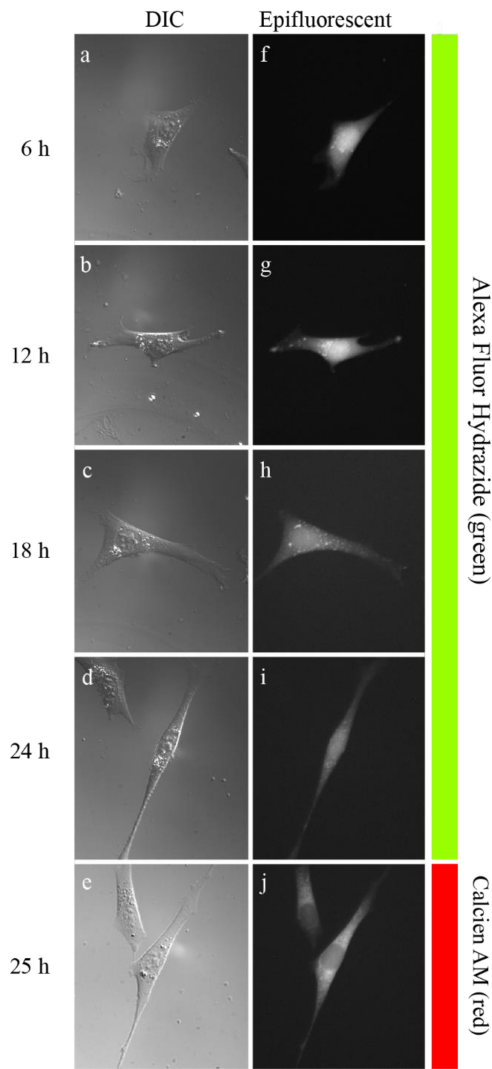


Fig. 8. Cytoplasmic SCE viability test. Viable cells, following cytoplasmic SCE, were observed over 25 h. An example of a cell targeted using cytoplasmic SCE is shown. Images collected using (a–e) DIC and (f–j) epifluorescent microscopy were collected in six h intervals. Green fluorescing dye is observed in the manipulated cell. (j) At 25 h, cells were exposed to calcein red. Viable cells were identified by continuous observation over 24 h and by observing calcein production in the cell after 1 h incubation in calcein AM.

TABLE III
VIABILITY ANALYSIS FOR CYTOPLASMIC SCE SITES

Set	SCE Site	N	Pulse freq. (Hz)	V _{SCE} (V)	\bar{t}_{SCE} (s)	t _{SCE SD} (s)	24-hr viable %
7	Cyto	10	10	-6	26.5	14.8	60.0
8	Cyto	10	40	-6	2.4	1.5	60.0

and for each parameter set the average viability was also 60% ($N = 10$ for each). The data are summarized in Table III.

IV. DISCUSSION AND FUTURE WORK

The system, methods, and instrumentation proposed in this study are intended to provide a seamless transition between the three, sequential stages of automated SCE including localization of cells and SCE sites, tip-membrane contact detection, and

SCE. Our method is capable of precise and repeatable targeting of thin, adherent cells for electroporation with an accuracy of nearly 100% success (see Table I). Our technology achieved new milestones in automated SCE.

Adherent cells less than 10 μm and SCE sites were localized using our machine vision algorithm described in [19]. Tip-membrane contact detection was executed using a statistical process control algorithm developed in [18] and visual feedback was implemented during nucleic and cytoplasmic SCE. In this discussion, we identify a site-specific dependence contributing to the success of SCE and identify areas of future work to improve the existing methods.

Targeted delivery of molecules, using SCE, is an effective means for conducting manipulation assays requiring greater access to cellular regions such as the nucleic and cytoplasmic SCE sites. However, little is known or has been reported on what region of the cell is best suited for SCE of macromolecules and specifically DNA of up to 14 kb/s [3]. When the microcapillary was placed over the nucleus, a success rate of 96.5% electroporation of the dye was achieved (see Table I) and was 19.0% successful at transfection of the plasmid DNA (see Table II) for all cells, which is similar to manual efficiencies [2], [3]. However, when regions lateral to the nucleus are targeted (i.e., cytoplasmic sites), a success rate of 86.9% electroporation of the dye is achieved and no successful electroporation of plasmid DNA ($n = 100$) was detected even though subsequent viability tests demonstrated 60% of the cells remained viable 24 h after SCE (see Table III). This demonstrates that the site placement of the microcapillary is a critical factor in successful SCE, and to the best of our knowledge, has not been previously reported in the literature.

Detecting tip-membrane contact is a critical event when processing thin cells to avoid rupturing the cells and breaking the microcapillary tip. At the beginning of each run, a measure of the noise σ was acquired relating noise levels to, λ and ν . As σ varies, the value of λ is scaled accordingly and is less susceptible to fluctuations in noise causing false contact detections. The residual, $x_k - \mu_0$, is normalized with σ , and samples must satisfy $y_k > \lambda$ or $-y_k > \lambda$ to increase C_k^+ or C_k^- , respectively. Variability in σ can influence the indentation distance (i.e., number of samples before the threshold is exceeded) as a low SNR will reduce the ability to discern a change from μ_0 . Greater control and system versatility could be achieved by implementing a control routine in response to variations in σ . Previous tip-membrane approach sequences, or simulated approach sequences based on a model of tip and membrane could be processed between runs to control the number of samples to achieve an alarm condition in response to variations in σ that occur. Performance surfaces, similar to those created during the calibration routine, could be generated or updated each sequence and incorporated with optimization routines to estimate more efficient parameters. Minor adjustments to λ and ν would be updated prior to the next run.

Differences in the compliance between cells and cell structures (e.g., nucleic and cytoplasmic SCE sites) could vary the rate of the formation of a seal. Thus, it is possible for variations between cells and cell lines to influence the tip-membrane

approach sequence. We tested our tip-membrane contact and SCE algorithm briefly on other cell lines including human breast cancer cells (MCF-7) and mouse neural blastoma cells (SH-SY5Y) with positive success. Although an extensive study was not performed, no significant differences were observed in comparison to NIH/3T3 cells during the tip-membrane contact algorithm or SCE while inserting fluorescing molecules. Establishing an electromechanical model of the seal created between a tip and a membrane would be a valuable contribution in future work for microcapillary-based, microelectrode methods of manipulation. This model could be experimentally verified using atomic force microscopy, and provide greater insight and to subtle differences encountered during the seal formation between cells, cell structures, and various cell lines.

Visual feedback was used during SCE which provided an effective indicator for SCE conditions and a suitable endpoint of the automated sequence. Where the light-collecting, capacity of the microscopy methods permits, future methods could visualize SCE using the molecules (e.g., DNA) attached directly to fluorescent molecules indicating SCE. Alternatively, conventional methods [2], [3] of SCE without visual indicators could be applied by modifying *Stage 3*, but lack visual feedback of molecules entering the cell and is nonspecific where the variability observed in \bar{t}_{SCE} indicates SCE varies from cell to cell (see Tables II, and III).

The methods in this study were designed to manipulate thin, adhered cells, allowing cell analysis over extended durations. The utility of the system could be increased by adapting similar infrastructure such as holding microcapillaries [9] or mechanical restraints [10], [12] to restrain and manipulate suspended cells similar to sizes used in this study ($h_C < 10 \mu\text{m}$). Alternatively, chemical methods (e.g., Poly-D-lysine, Poly-L-lysine) may offer a simple method, where cells can be restrained sufficiently on conventional glass or plastic substrates.

V. CONCLUSION

SCE has the potential to drive single cell research where accuracy, repeatability, and higher-than-manual throughput are required. Our system provides a versatile, automated solution with capabilities of accurately localizing cytoplasmic or nucleic SCE sites on single cells and inserting exogenous molecules into cell features with micrometer thicknesses via SCE. Our system exceeded the throughput of manual SCE by reducing the cell processing rate to one-third (81 s/cell) in comparison to rates reported in the literature (e.g., 480 s/cell [5] and 240 s/cell [6]). In addition, we provided a visual feedback to monitor the progress of SCE and reported a site-specific dependence in the transfection ratio when targeting cytoplasmic SCE sites and nucleic SCE sites.

The instrumentation and methods described are intended to provide the framework for a powerful method of manipulation to the scientific community. The engineered architecture is intended as a significant stepping stone in the development of future designs to provide even greater capabilities and a broader selection of methods not achievable by manual processes. While a complete solution for automated SCE has been presented, it is

the opinion of the authors that the technology is only in its infancy and the true power of SCE has yet to be unleashed. Further optimization of our routines, and maturation of automated SCE in general, will inevitably improve the efficiency and latencies of cell-processing reported in this study.

REFERENCES

- [1] N. Blow, "Journeys across the membrane," *Nat. Methods*, vol. 6, no. 4, pp. 305–309, Apr. 2009.
- [2] K. Haas, W. C. Sin, A. Javaherian, Z. Li, and H. T. Cline, "Single-Cell electroporation for gene transfer *in vivo*," *Neuron*, vol. 29, no. 3, pp. 583–591, 2001.
- [3] J. Rae and R. Lewis, "Single-cell electroporation," *Pflügers Arch.*, vol. 443, no. 4, pp. 664–670, Feb. 2002.
- [4] P. Lovell, S. H. Jezzini, and L. L. Moroz, "Electroporation of neurons and growth cones in *Aplysia California*," *J. Neurosci. Methods*, vol. 151, no. 2, pp. 114–120, Mar. 2006.
- [5] M. Wang, O. Orwar, and S. G. Weber, "Single-cell transfection by electroporation using an electrolyte/plasmid-filled capillary," *Anal. Chem.*, vol. 81, no. 10, pp. 4060–4067, May 2009.
- [6] M. Tanaka, Y. Yanagawa, and N. Hirashima, "Transfer of small interfering RNA by single-cell electroporation in cerebellar cell cultures," *J. Neurosci. Methods*, vol. 178, no. 1, pp. 80–86, 2009.
- [7] E. Neumann, S. Kakorin, and K. Toensing, "Fundamentals of electroporative delivery of drugs and genes," *Bioelectrochem. Bioenerg.*, vol. 48, no. 1, pp. 3–16, 1999.
- [8] K. Nolkrantz, C. Farre, A. Brederlau, R. L. Karlsson, C. Brennan, P. S. Eriksson, S. G. Weber, and O. Orwar, "Electroporation of single cells and tissues with an electrolyte-filled capillary," *Anal. Chem.*, vol. 73, pp. 4469–4477, 2001.
- [9] Y. Sun and B. J. Nelson, "Biological cell injection using an autonomous microrobotic system," *Int. J. Robot. Res.*, vol. 21, no. 10/11, pp. 861–868, 2002.
- [10] H. Huang, D. Sun, J. K. Mills, and S. H. Cheng, "Integrated vision and force control in suspended cell injection system: Towards automatic batch biomanipulation," in *Proc. IEEE Conf. Robot. Autom.*, 2008, pp. 3413–3418.
- [11] Y. Xie, D. Sun, H. Y. G. Tse, C. Liu, and S. H. Cheng, "Force sensing and manipulation strategy in robot-assisted microinjection on zebrafish embryos," *IEEE Trans. Mechatronics*, vol. 16, no. 6, pp. 1002–1010, Dec. 2011.
- [12] W. Wang, X. Liu, D. Gelinas, B. Ciruna, and Y. Sun, "A fully automated robotic system for microinjection of zebrafish embryos," *Plos One*, vol. 2, no. 9, p. e862, Sep. 2007.
- [13] H. Huang, D. Sun, J. K. Mills, W. J. Li, and S. H. Cheng, "Visual-based impedance control of out-of-plane cell injection systems," *IEEE Trans. Autom. Sci. Eng.*, vol. 6, no. 3, pp. 565–571, Jul. 2009.
- [14] W. Wang, Y. Sun, M. Zhang, R. Anderson, L. Langille, and W. Chan, "A system for high-speed microinjection of adherent cells," *Rev. Sci. Instrum.*, vol. 79, no. 10, p. 104302, 2008.
- [15] C. Bae and P. Butler, "Automated single-cell electroporation," *BioTechniques*, vol. 41, no. 4, pp. 399–402, Oct. 2006.
- [16] P. Kallio, T. Ritala, M. Lukkari, and S. Kuikka, "Injection guidance system for cellular microinjections," *Int. J. Robot. Res.*, vol. 26, pp. 1303–1313, 2007.
- [17] K. Sakaki, N. Dechev, R. D. Burke, and E. J. Park, "Development of an autonomous biological cell manipulator with single-cell electroporation and visual servoing capabilities," *IEEE Trans. Biomed. Eng.*, vol. 56, no. 8, pp. 2064–2074, Aug. 2009.
- [18] K. Sakaki, H. Esmailsabzali, N. Dechev, R. D. Burke, and E. J. Park, "A generalized tip-membrane contact detection algorithm for automated single cell electroporation using statistical process control," *IEEE Trans. Autom. Sci. Eng.*, vol. 9, no. 2, pp. 226–236, Apr. 2012.
- [19] H. Esmailsabzali, K. Sakaki, N. Dechev, R. D. Burke, and E. J. Park, "Machine vision-based localization of nucleic and cytoplasmic injection sites on low-contrast adherent cells," *Med. Biol. Eng. Comput.*, vol. 50, no. 1, pp. 11–21, Sep. 2012.
- [20] E. S. Page, "Continuous inspection schemes," *Biometrika*, vol. 41, pp. 100–115, Jun. 1954.
- [21] M. Basseville and I. V. Nikiforov, *Detection of abrupt change theory and applications*. Englewood Cliffs, NJ, USA: Prentice-Hall, 1993.

- [22] J. O. Westgard, T. Groth, T. Aronsson, and C. H. De Verdier, "Combined Shewhart-cusum control chart for improved quality control in clinical chemistry," *Clin. Chem.*, vol. 23, no. 10, pp. 1881–1887, 1977.
- [23] D. C. Montgomery, *Introduction to Statistical Quality Control*, 4th ed. New York, NY, USA: Wiley, 2001.
- [24] *P-1000 & P-97 Pipette Cookbook 2011*. Sutter Instrument Company Novato, CA, USA, 2011.
- [25] R. E. Campbell, O. Tour, A. E. Palmer, P. A. Steinbach, G. S. Baird, D. A. Zacharias, and R. Y. Tsien, "A monomeric red fluorescent protein," *Proc. Natl. Acad. Sci.*, vol. 99, no. 12, pp. 7877–7882, 2002.



Kelly Sakaki (M'09) received the Telecommunications Engineering Technologist Diploma degree from the Northern Alberta Institute of Technology, Edmonton, AB, Canada, in 2001, the B.Eng. degree in computer systems engineering, and the M.A.Sc. degree in mechanical engineering from the University of Victoria, Victoria, BC, Canada in 2005 and 2007, respectively, and the Ph.D. degree in mechatronic systems engineering from the School of Engineering Science, Simon Fraser University, BC, Canada, in December 2012. He has recently joined the Brain Research Centre at the University of British Columbia, Vancouver, BC, Canada, as a Postdoctoral Fellow.

His research interests include automation, electrical and mechanical design, signal processing, and machine vision. He is currently investigating novel methods of single cell analysis and manipulation using robotics-assisted instrumentation, microfluidics and MEMS.



Gratien G. Prefontaine received the B.Sc. degree, the M.Sc. degree and the Ph.D. degree in biochemistry in 1993, 1996, and 2001, respectively, all from the University of Ottawa, Ottawa, ON, Canada.

From 2001 to 2008, he was engaged in Postdoctoral Research Training at the University of California, San Diego, USA, and he became an Assistant Project Scientist in 2007. He is currently an Assistant Professor in the Faculty of Health Sciences, Simon Fraser University Burnaby, BC, Canada, and he is also an Associate Member in the Faculty of Science,

Departments of Molecular Biology and Biochemistry as well as Biological Sciences. His research interests include gene regulation, DNA methylation, DNA pyrosequencing, microarray technology, bacterial artificial chromosome recombination technology, and developmental biology.



Nikolai Dechev (M'04) received the B.A.Sc., M.A.Sc., and the Ph.D. degrees in 2004, all from the Department of Mechanical Engineering, University of Toronto, Toronto, Canada, in 1996, 1999, and 2004, respectively.

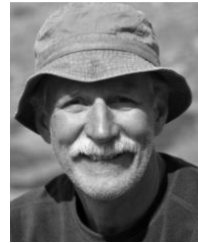
He is currently an Associate Professor in Mechanical Engineering at the University of Victoria, Victoria, BC, Canada. His research interests include biomedical systems design in the areas of advanced hand prosthesis, implantable sensors and prosthesis control, MEMS sensors, and robotic micromanipulation and automation technologies for MEMS and biological cells.

Dr. Dechev is a Member of the ASME.



Hadi Esmaeilsabzali received the B.A.Sc. degree in biomedical engineering from the School of Medicine, Shahid Beheshti University of Medical Sciences, Tehran, Iran, in 2003 and the M.A.Sc. degree in control engineering from the School of Electrical Engineering, Iran University of Science and Technology, Tehran, Iran, in 2006. He is currently working toward the Ph.D. degree in mechatronic systems engineering from Simon Fraser University, BC, Canada.

His research interests include immunomagnetic cell manipulation, development of lab-on-a-chip bioMEMS for rare-cell detection, isolation, characterization and point-of-care testing devices, single-cell biomaniulation, and machine vision applied to these areas.



Robert D. Burke received the B.Sc. (Hons.) degree, and the Ph.D. degree in 1978, both from the University of Alberta, Edmonton, Canada, in 1974 and 1978, respectively.

He has been at the University of Victoria, Victoria, BC, Canada since 1980, and is currently the Chair of the Department of Biochemistry and Microbiology. His research interests include cellular and developmental biology. He has published more than 100 journal papers in these areas.



Shabnam Massah received the B.Sc. degree in cell and molecular biology (microbiology), from Azad University of Karaj, Karaj, Iran, in 2006. She is currently working toward the Ph.D. degree in the Faculty of Health Sciences, Simon Fraser University Burnaby, BC, Canada.

Her research interests include understanding the role of epigenetic modifications, specifically, DNA methylation in regulation of gene expression. She is also interested in identification of molecules that can interpret or sense chromatin modifications, and maintain the normal or disease-related gene expression profiles.



Edward J. Park (M'03) received the B.A.Sc. degree from the University of British Columbia, Vancouver, BC, Canada, and the M.A.Sc. and the Ph.D. degrees from the University of Toronto, Toronto, Canada, in 1996, 1999, and 2003, respectively, all in mechanical engineering.

Previously, he was an Assistant Professor at the Department of Mechanical Engineering, University of Victoria, Victoria, BC, Canada, from 2003 to 2008. He is currently an Associate Professor of the School of Mechatronic Systems Engineering at the Simon

Fraser University, Surrey, BC, Canada, and the Director of the Biomechatronic Systems Laboratory. He is also an Associate Member of the Faculty of Health Sciences. He has authored/coauthored more than 80 journal and conference papers in these areas. His current research interests include biomechatronics and biomedical technologies for life sciences, rehabilitation and medicine, and mechatronics applied to next generation vehicular, robotic, and space systems.